Graphitic C_6N_6-supported Dual Cu/Zn Single-Atom Catalyst Mimicking Allosteric Regulation for Intelligent Switching Biosensing

Qing Hong,[1] Caixia Zhu,[1] Kaiyuan Wang,[1] Wang Li,[1] Yuan Xu[1], Kaiqing Wu[1], Zhuang Wang,[1] Zhixin Zhou,[1] Yanfei Shen*[2], Songqin Liu,[1] Yuanjian Zhang*[1]

[1]Jiangsu Engineering Laboratory of Smart Carbon-Rich Materials and Device, Jiangsu Province Hi-Tech Key Laboratory for Bio-Medical Research, School of Chemistry and Chemical Engineering, Southeast University, Nanjing 211189, China, Email: Yuanjian.Zhang@seu.edu.cn

[2]Medical School, Southeast University, Nanjing 210009, China, Email: Yanfei.Shen@seu.edu.cn

Abstract

Self-adaptability is highly envisioned for artificial devices such as robots with chemical noses. To this end, seeking catalysts with reversibly switchable functions is promising but generally hampered by mismatched initial valence state of transition metal active centers and electronic structures. Herein, we report a graphitic C_6N_6-supported dual Cu/Zn single-atom catalyst with a synergistic effect (Cu/Zn-C_6N_6). It could not only rely on the Cu(I)/Cu(II) redox reaction with promotion from Zn to exhibit a remarkable superoxide dismutase-like (SOD) performance, but also activate Cu(I)/Cu(0) redox reaction to highly switch a marginable peroxidase-like (POD) activity, in which the initial oxidation state was transformed by a photoreduction. The multiformity of the cycles between different valence states for the same catalytic active center makes the reaction activity capable of being reversible switch, the switch efficiency can reach more than 90%. As a proof-of-concept application, Cu/Zn-C_6N_6 was further confined to a microfluidic chip and applied to a single-interface biosensor with reversibly switched ability in detecting xanthine and glucose in vitro.

Introduction

Metabolic process plays an important role in living organisms to maintain diverse life activities. In general, the intricate metabolic reactions require regulatory mechanisms to prevent metabolic disorders. For example, high blood sugar prompts pancreatic beta cells to release insulin, which activates glycogen synthase to build glycogen and inhibits its breakdown, while low levels do the opposite, all controlled by phosphorylation.[1] It features the highly reversible switch of distinctive functions triggered by allosteric regulation. For the same reason, mimicking such allosteric regulation is highly envisioned for next generation of intelligent sensors for multiple types of chemical signals meanwhile maintaining high specificity at a single sensing interface,[2-5] but remains a formidable task.

Single-atom enzymes (SAzymes), as a new artificial enzyme, possesses both the physical and chemical properties of nanomaterials and enzymatic catalytic activity.[6-16] They have shown great application prospects in diverse fields, such as biosensors,[17-20] immunoassays,[21-25] and cancer therapeutics.[26-32] However, the rigid molecular structure of most SAzymes results in a lack of conformational regulation functions.[33, 34] To overcome this limitation, several interesting works of coupling extrinsic supramolecules or photo-responsive groups such as azobenzene, have been reported,[35-37] which successfully modulates a particular enzyme-like activity on and off. Nonetheless, realizing the full potential of allosteric regulation mimicking hinges on conquering the critical hurdle of enabling switching between distinct types of activities.

It is worth noting that transition metal-based SAzymes could drive a biomimetic catalytic reaction via redox of metal centers,[38-46] which is similar to the action of natural metalloenzymes. However, the mismatch between the initial valence state of transition metal active centers and electronic structures requiring for a certain catalytic behavior generally exists in different catalytic pathways,[47-52] limiting the efficient and reversible conversion among multiple functions. To this end, we reason that manipulating oxidation states of metal centers for different redox reactions would offer a simple and effective way to adjust the overall electronic structure, thus mimicking the allosteric

mechanism and realizing a reversible switch of functions; however, it has been rarely reported.

Herein, we report a graphitic C_6N_6-supported dual Cu/Zn SAzyme (Cu/Zn-C_6N_6) with switchable functions triggered by light irradiation. Cu/Zn-C_6N_6 exhibited a remarkable superoxide dismutase (SOD)-like activity and a marginable peroxidase-like (POD) activity under dark; while it completely reversed under light irradiation. Moreover, such switch between SOD- and POD-like activities were reversible by alternating dark and light irradiation. Comprehensive experiments and theoretical calculations verified the SOD- and POD-like activities originated from the same active center (Cu-N_x). However, the former relied on the Cu(I)/Cu(II) redox reaction with promotion from Zn, while the latter was based on the Cu(I)/Cu(0) redox reaction, in which the initial oxidation state was transformed by a photoreduction. As a proof-of-concept application, Cu/Zn-C_6N_6 was further confined to a microfluidic chip and applied to a single-interface biosensor with reversibly switched ability in detecting xanthine and glucose in vitro.

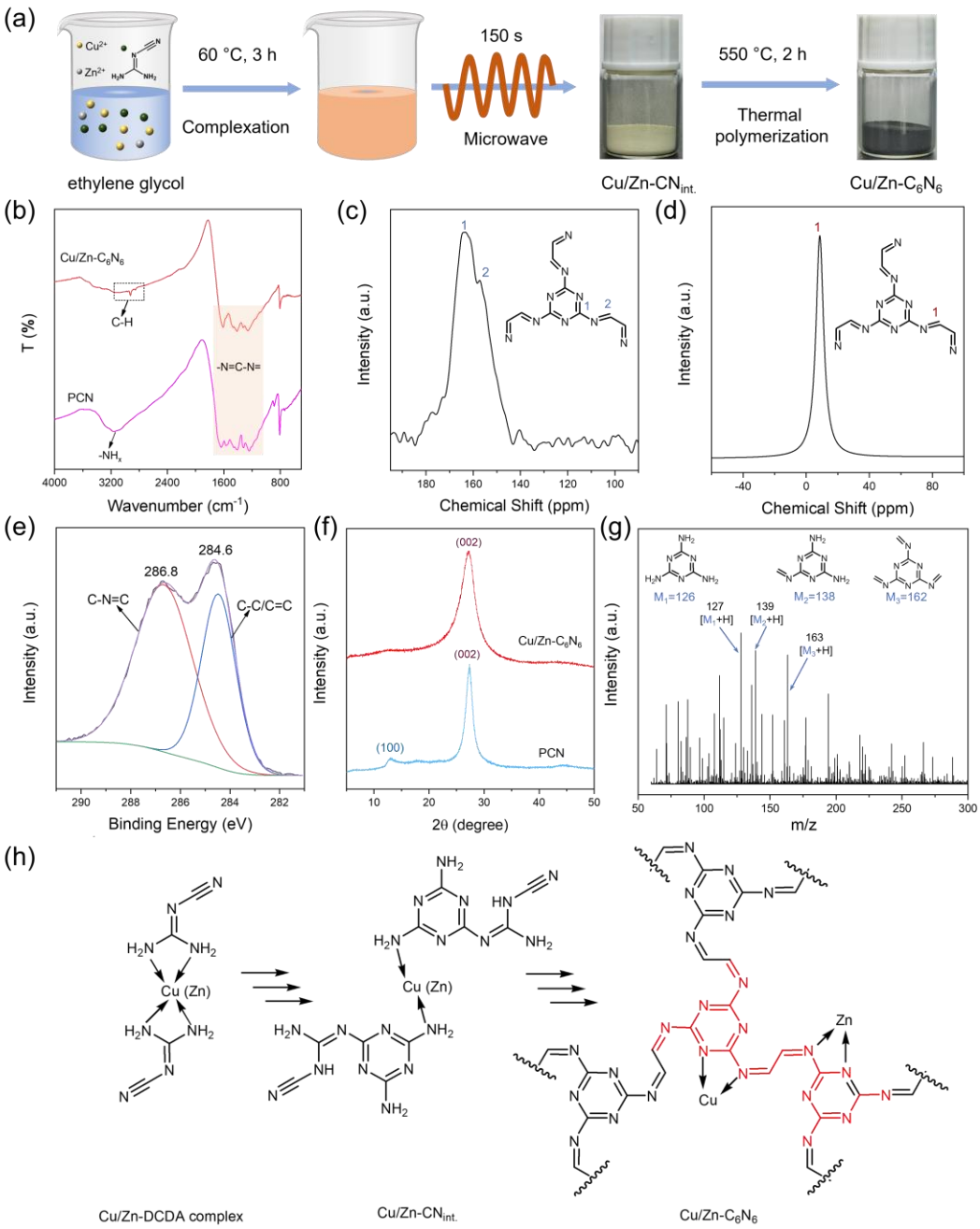

Fig. 1 Preparation and molecular structure of Cu/Zn-C_6N_6. (a) Brief Synthesis procedure for Cu/Zn-C_6N_6. (b) FT-IR spectra of Cu/Zn-C_6N_6 and PCN. Solid-state (c) ^{13}C and (d) ^{1}H NMR spectra of Cu/Zn-C_6N_6. (e) C 1*s* XPS spectrum of Cu/Zn-C_6N_6. (f) Normalized XRD patterns of Cu/Zn-C_6N_6 and PCN. (g) LDI-TOF mass spectrum of Cu/Zn-C_6N_6. (h) Proposed condensation processes and molecular structure of Cu/Zn-C_6N_6.

Results and Discussion

Synthesis and molecular structure of Cu/Zn-C_6N_6

Cu/Zn-C_6N_6 was prepared according to the previously reported literature.[45] As shown in **Fig. 1a**, copper acetate and zinc acetate were selected to coordinate with dicyandiamide (DCDA) in ethylene glycol (EG) solution at 60 ℃, forming a brown Cu/Zn-DCDA complex. Subsequently, microwave-assisted polymerization was carried out to form a pale-yellow Cu/Zn-CN intermediate,[53] denoted as Cu/Zn-CN_{int}. Finally, the obtained Cu/Zn-CN_{int} was further thermally polymerized in a muffle furnace at 550 ℃ to fabricate Cu/Zn-C_6N_6. As a comparison, Cu-C_6N_6 and Zn-C_6N_6 were also fabricated by the same microwave-assisted condensation and thermal polymerization with the individual Cu and Zn coordinated DCDA in EG.

The combustion elemental analysis (**Table S1**) showed the molar C/N ratio in Cu/Zn-C_6N_6 was approximately 1. The FTIR spectrum demonstrated the chemical structure of the novel carbon nitride. As shown in **Fig. 1b**, both conventional polymeric carbon nitride (PCN) and Cu/Zn-C_6N_6 exhibited two strong vibration characteristic peaks around 800 cm^{-1} and 1200-1700 cm^{-1}, corresponding to the typical triazine ring (CN heterocycle) structure in the CN skeleton.[54] In addition, an unusual stretching vibration peak around 2900 cm^{-1} was observed in Cu/Zn-C_6N_6, which can be assigned to the stretching characteristic peak of the C-H bond.[55] The solid-state NMR spectroscopy was used to further explore the nature of the building blocks of Cu/Zn-C_6N_6. As illustrated in **Fig. 1c**, the spectrum depicted two characteristic carbon atom peaks, the first one appearing at around 163 ppm was assigned to the carbon atoms in the triazine ring units, proving the existence of conjugated triazine ring structures. The second peak at approximately 156 ppm was ascribed to the carbon atom indirectly connected to the triazine ring.[56] Those two types of carbon atoms and C-H bond in the NMR spectra confirmed the existence of triazine rings and non-cyclization groups of -N=CH- in the skeleton of Cu/Zn-C_6N_6. The ^1H magic angle spinning (MAS) NMR spectrum (**Fig. 1d**) was also carried out to confirm the local environment of the H atom. A single characteristic peak approximately at around 8.3 ppm was observed, which corresponded to the non-cyclization groups of -N=CH-. It is worth noting that this

chemical shift often corresponded to an aromatic carbon behavior,[57] demonstrating that the second carbon atom exhibited a conjugation effect with the triazine ring structure.

The high-resolution X-ray photoelectron spectroscopy (XPS) was performed to determine the additional binding information of Cu/Zn-C_6N_6. As shown in **Fig. 1e**, the C1s XPS spectrum showed two characteristic peaks at around 284.6 eV (C1) and 286.8 eV (C1), respectively, corresponding to the C-C peak and C species in triazine rings (C−N=C).[58] Notably, the C-C peak (ca. 284.6 eV) in PCN was ascribed to random adventitious carbon, and the C-$(N)_3$ shifted to a high binding energy at 288.1 eV (**Fig. S1**).[59] These results indicated that the non-cyclization groups of -N=CH- were coupled in the thermal polymerization process to form -N=CH-CH=N- groups. The crystal structure of Cu/Zn-C_6N_6 was further analyzed by XRD. As a control, the XRD pattern of PCN was also determined. As shown in **Fig. 1f**, PCN showed two strong characteristic peaks at 2θ = 13.4° and 27.6°, corresponding to in-plane structural packing (100) and interlayer stacking reflection (002), respectively. While for Cu/Zn-C_6N_6, the diffraction peak was broadened and down-shifted around at 2θ =26.0°, indicating a slightly enlarged interlayer spacing owing to the insertion of Cu and Zn atoms between C_6N_6 layers. Furthermore, the peak (100) in Cu/Zn-C_6N_6 was negligible, suggesting weakened crystallinity.

The matrix-free laser desorption/ionization time-of-flight (LDI-TOF) mass spectra were further performed to identify the precise molecular structure of Cu/Zn-C_6N_6. **Fig. 1g** exhibited a series of m/z peaks derived from the ablation products of the repetitive C_6N_6 units. The m/z [M + H^+] of 127.11 was ascribed to $C_3N_6H_6$ (M_1, melamine, calc.: 126), m/z [M + H^+] of 139.15 was assigned to $C_4N_6H_6$ (M_2, calc.: 138), and m/z [M + H^+] of 163.34 was corresponding to $C_6N_6H_6$ (M_3, calc.: 162). The other m/z peaks displayed in **Fig. S2**, also suggested the ablation unit's information. As a result, the above all structural explorations indicated that Cu/Zn-C_6N_6 featured a repetitive basic triazine ring and a non-cyclization linker of -N=CH-CH=N-. The possible polymerization processes and the molecular structure of Cu/Zn-C_6N_6 were shown in **Fig. 1h**.

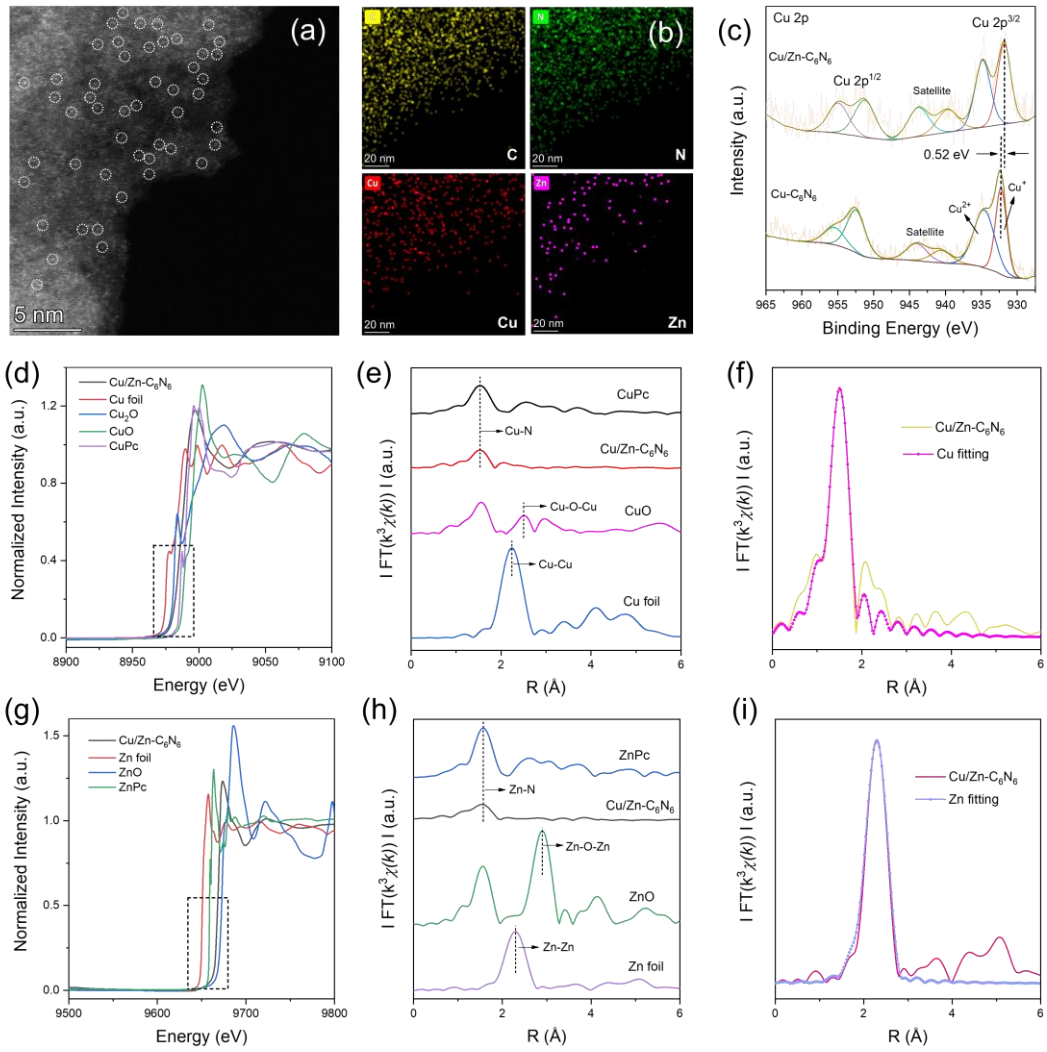

Fig. 2 Morphologies and synchrotron XAFS measurements of Cu/Zn-C_6N_6. (a) HAADF-STEM and (b) STEM-EDS images of Cu/Zn-C_6N_6. (c) Cu 2*p* XPS spectrum of Cu/Zn-C_6N_6 and Cu-C_6N_6. (d) Cu k-edge XANES profiles of Cu foil, Cu_2O, CuO, Cu/Zn-C_6N_6, and CuPc. (e) Cu k-edge EXAFS spectra in R-space of the Cu/Zn-C_6N_6, CuPc, CuO and Cu foil samples. (f) EXAFS fitting curve of Cu k-edge for Cu/Zn-C_6N_6 in R-space. (g) Zn k-edge XANES profiles of Zn foil, ZnO, Cu/Zn-C_6N_6, and CuPc. (h) Zn k-edge EXAFS spectra in R-space of the Cu/Zn-C_6N_6, CuPc, CuO and Cu foil samples. (i) EXAFS fitting curve of Zn k-edge for Cu/Zn-C_6N_6 in R-space.

Cu and Zn single-atom structure of Cu/Zn-C_6N_6

As shown in **Fig. S3**, the scanning electron microscope (SEM) images of Cu/Zn-C_6N_6 exhibited a continuously microporous structure. The high-resolution transmission

electron microscopy (HR-TEM) images (**Fig. S4**) of Cu/Zn-C_6N_6 at different resolutions displayed a thin layered nanosheet with no obvious adhesion of Cu/CuO and Zn/ZnO nanoparticles on the surface of the C_6N_6 nanosheets, which is consistent with the XRD results. In addition, the size of Cu/Zn-C_6N_6 nanosheets from the dynamic light scattering (**Fig.S5**) was mainly distributed around 100 nm, consistent with the results of HR-TEM. Further, the high-angle annular darkfield scanning transmission electron microscopy (HAADF-STEM) was performed to confirm the local distribution of Cu and Zn atoms. **Fig. 2a** displayed a dense distribution of uniformly single-atom Cu and Zn on the C_6N_6 matrix, evident by abundant isolated bright spots highlighted by a white circle (more images at random position were given in **Fig. S6)**. Notably, it was hard to identify Cu and Zn atoms due to their close atomic numbers. The mass loading of Cu and Zn were quantitatively measured to be 1.44 and 0.34 wt%, respectively, by inductively coupled plasma optical emission spectroscopy (ICP-OES). The corresponding high-resolution STEM-EDS elemental mapping images confirmed the C, N, Cu and Zn species were isolated and atomically dispersed across the entire C_6N_6 nanosheet (**Fig. 2b**).

Owing to the HR-TEM and HAADF-STEM were difficult to accurately recognize the state of metal species, the X-ray photoelectron spectroscopy (XPS) was carried out to give further insight. As shown in **Fig. S7**, the survey XPS spectrum exhibited the existence of C, N, Cu, Zn, and O elements in the Cu/Zn-C_6N_6. Accordingly, the high-resolution Cu 2p spectrum (**Fig. 2c** and **Fig. S8**) displayed two main peaks with a binding energy of 933.0 eV (Cu $2p^{3/2}$) and 953.0 eV (Cu $2p^{1/2}$), and the corresponding satellites at around 944.8 eV demonstrated the existence of Cu^{2+} species in Cu/Zn-C_6N_6. In detail, the peaks at 933.0 eV (Cu $2p^{3/2}$) can be deconvoluted into two peaks at around 931.9 and 934.8 eV, assigned to Cu^{1+} and Cu^{2+}, respectively.[60, 61] Similarly, the high-resolution Zn 2p spectrum in **Fig. S9** showed two main peaks at 1021.7 eV and 1044.8 eV, which were assigned to Zn $2p^{3/2}$ and Zn $2p^{3/2}$, respectively, suggesting that the oxidation state of Zn single atom was Zn^{2+}.[31, 62] For comparison, the control sample of Cu-C_6N_6 was also prepared. Interestingly, the binding energy (BE) of Cu $2p^{3/2}$ and Cu

$2p^{1/2}$ in Cu/Zn-C_6N_6 were shifted by 0.52 eV toward a lower BE (**Fig.2c**), with respect to that of Cu-C_6N_6.[63, 64] In general, the Zn atoms could donate their outer electrons to the Cu atoms, owing to the lower electronegativity of Zn (c=1.65) than Cu (c=1.90).[62] Such interactions between Cu and Zn atoms would tune the electronic structure, generating optimal active sites for both reactant adsorption and intermediate desorption during catalysis.

To further acquire the chemical state and coordination chemistry of Cu/Zn-C_6N_6, the X-ray absorption fine structure (XAFS) measurements of the Cu K-edge were performed. The Cu K-edge X-ray absorption near-edge structure (XANES) curves in **Fig.2d** exhibited the Cu/Zn-C_6N_6 was located those of Cu foil and CuO, indicating that the Cu atoms carried a partial positive charge between 0 and +2, which corresponded to the XPS spectrum (**Fig.2c**).[65] The Fourier transform (FT) k^3-weighted $\chi(k)$-function curves of the Cu K-edge extended X-ray absorption fine structure (EXAFS) spectrum in R space were displayed in **Fig.2e**. Compared with the reference Cu foil, CuO and CuPc, Cu/Zn-C_6N_6 showed a characteristic peak located at around 1.5 Å, which was mainly assigned to the Cu-N first coordination shell rather than the metallic Cu-Cu and Cu-O-Cu interaction at ≈2.2 and 2.7 Å.[66] It corresponded with the HAADF-STEM images, indicating that the Cu atoms in the C_6N_6 matrix were atomically dispersed. The detailed structural information was revealed in EXAFS fitting (**Fig.2e and Table S2**). The bond length and coordinated number between Cu and N were approximately 1.96 Å and 2, The above fitting analysis confirmed that the isolated and atomically dispersed Cu atoms were coordinated by two N atoms.

More structural information of Zn was revealed by the XAFS measurements of the Zn K-edge. As shown in **Fig. 2f**, the Zn K-edge XANES curves exhibited the near-edge absorption close to ZnO, suggesting the valence states of Zn in Cu/Zn-C_6N_6 was about +2,[67] in agreement with the XPS analysis. The FT-EXAFS spectra (**Fig. 2h**) displayed a main peak at around 1.54 Å, which was assigned to the Zn-N first scattering path.[68] Notably, there was no obvious peaks of metallic Zn-Zn and Zn-O-Zn interaction at ≈2.2 and 2.8 Å, respectively, confirming that Zn atoms were isolated and atomically

dispersed in the C_6N_6 framework. The EXAFS fitting in **Fig. 2i** and **Table S3** recovered the Zn-N_2 coordination in Cu/Zn-C_6N_6 (Zn-N bond with a length of 2.02 Å).[62] The existence of Cu-N and Zn-N bonds was also complementarily confirmed by the N 1s XPS spectra (**Fig. S10**). Those results indicated that the atomically dispersed Cu-N_2 and Zn-N_2 moieties were predominated in the Cu/Zn-C_6N_6, which potentially provided optimal electronic structure for switchable SOD-/POD-like activities.

Switch between SOD-like and POD-like activity of Cu/Zn-C_6N_6

The filling of Cu/Zn-N_2 coordination into the C_6N_6 framework endowed it with a SOD-like activity under dark and a POD-like activity under light irradiation. The SOD-like activity of Cu/Zn-C_6N_6 was systematically evaluated by using a total SOD kit method,[29] in which the yellow reduction product of 2-(2-Methoxy-4-nitrophenyl)-3-(4-nitrophenyl)-5-(2,4-disulfophenyl)-2H-tetrazolium sodium salt (WST-8) to formazan by $O_2^{\bullet-}$ generated in the xanthine/xanthine oxidase (X/XOD) system was measured at 450 nm (**Fig. 3a** and **Fig. 3bc**). The addition of Cu/Zn-C_6N_6 in the system would disproportionate $O_2^{\bullet-}$, leading to a decrease in formazan production. Similarly, the POD-like activity was evaluated using catalytic oxidation of 2, 2'-azino-bis (3-ethylbenzothiazoline-6-sulfonic acid) (ABTS)[69] with H_2O_2 and monitoring the typical absorbance of the product at 417 nm (**Fig. 3a** and **Fig. 3bc**). As displayed in **Fig. 3b**, in dark, Cu/Zn-C_6N_6 displayed a high-efficiency elimination of $O_2^{\cdot-}$ via a dominated SOD-like performance (**Fig. S11 and Fig. S12**), while the POD-like activity was negligible. Further, when irradiated by a household white LED (400-900 nm, 50 mW/cm^2, **Fig. S13**), the POD-like catalytic activity of Cu/Zn-C_6N_6 was successfully switched, due to the narrow optical gap (1.10 eV, **Fig. S14 and 15**) which could effectively absorb natural light. As shown in **Fig. 3c**, a 30-fold increase of the absorbance of $ABTS_{ox}$ at 417 nm under light irradiation (0.54) and in the dark (0.018) was observed. At the same time, the absorbance of WST-8_{re} only showed a slight decrease, suggesting the SOD-like performance was remarkably inhibited. Those results demonstrated that Cu/Zn-C_6N_6 could not only eliminate $O_2^{\cdot-}$ through the SOD-like reaction but also switch to the POD-like activity in substrates oxidation under light

irradiation. **Fig. 3d** graphically exhibited a remarkable SOD-like activity and a marginable POD activity under dark, while it completely reversed under light irradiation, the switch efficiency could reach more than 90%, indicating the advanced switchable effect of those two distinct activities.

Considering that surrounding pH is often used to tune the catalytic properties of nanozymes,[70] the influence of pH on WST-8 reduction was also explored. As shown in **Fig. S16**, the SOD-like activity of Cu/Zn-C_6N_6 retained the inhibition and activation of enzyme activities in a wide pH range. These results demonstrated the highly switchable multienzyme activity of Cu/Zn-C_6N_6 was presumably originated from the intrinsic structural transformation of Cu/Zn-C_6N_6, rather than the reaction conditions (e.g., pH). The different molar ratio of Cu^{2+}/Zn^{2+} was investigated to obtain the optimal SOD-like and POD-like catalytic activity. As displayed in **Fig. S17**, with the increase of Cu^{2+}/Zn^{2+} molar ratio, the Δabs of WST-8_{re} displayed a volcano profile, indicating Zn atom acted as an auxiliary metal to enhance the SOD-like activity. However, the absorbance of $ABTS_{ox}$ decreased with the increase of Zn^{2+} concentration, which confirmed the large amount of Zn species occupied the light active site, resulting in the decrease of POD-like activity. As the Zn atom would transfer electrons to the Cu atom, Cu atom was the main active site towards SOD-like reaction. While in the POD-like reaction, Cu atom acted as the only active site to initiate the reaction. A series of controlled experiments were conducted to further eliminate potential interfering factors in the SOD-like and POD-like activity of Cu/Zn-C_6N_6 (**Fig. S18-S20**). In addition, the light-switched activity of Cu/Zn-C_6N_6 was able to easily modulate by tuning the irradiation power density (**Fig. S21**).

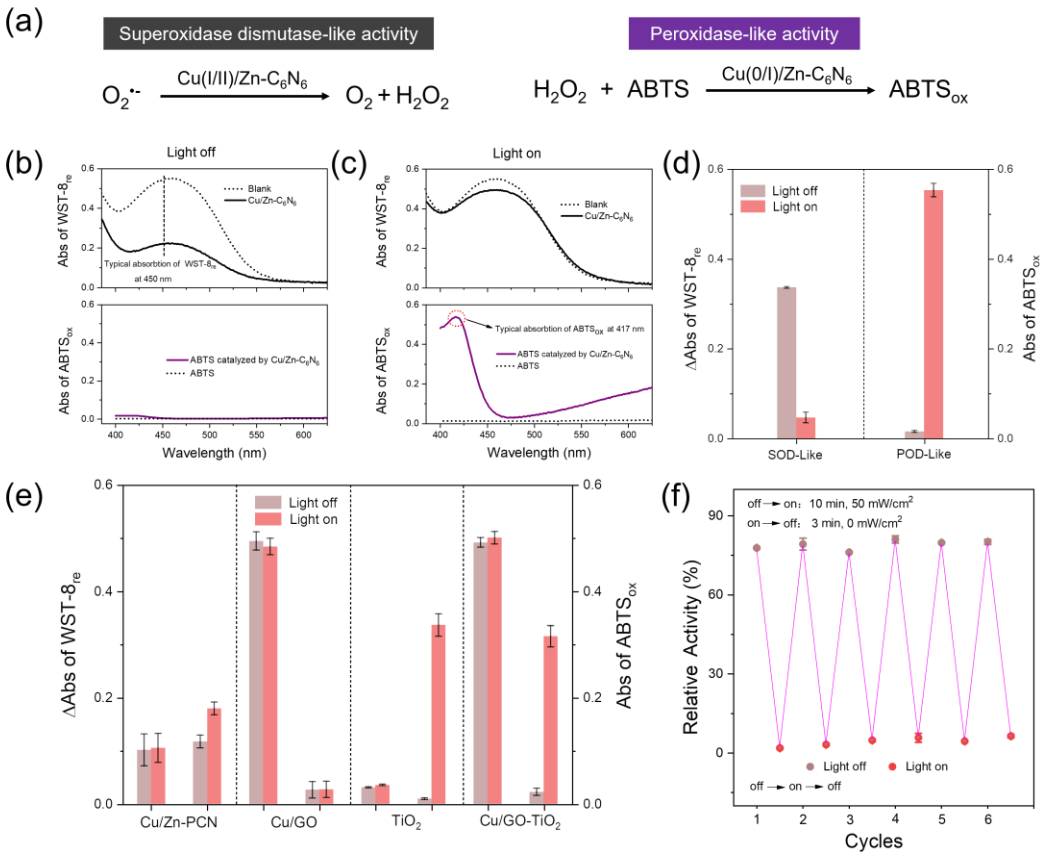

Fig. 3 Switchable SOD-/POD-like activities by alternating light on and off. (a) Equations of disproportionated reaction of $O_2^{\cdot-}$ and standard ABTS catalytic oxidation using Cu/Zn-C_6N_6. UV-vis absorption spectrum of WST-8_{re} and (c) $ABTS_{ox}$ catalyzed by Cu/Zn-C_6N_6 without and with light irradiation. ΔAbs of WST-8_{re} and abs of $ABTS_{ox}$ catalyzed by (d) Cu/Zn-C_6N_6, and (e) control Cu/Zn-PCN, Cu/GO, TiO_2 and Cu/GO-TiO_2 without and with light irradiation. (f) Cycling activity of Cu/Zn-C_6N_6 with alternating light irradiation on and off (irradiation time: 10 min, dark time: 3 min). Error bars represent the standard error derived from three independent measurements.

To consolidate the advanced switchable effect of those two distinct activities in Cu/Zn-C_6N_6, a series of controls, including Cu/Zn-based single-atom catalysts, Cu-containing SOD-like nanozyme, photo-responsive POD-like nanozyme, or their physical mixtures were contrasted. As shown in **Fig. 3d**, although Cu/Zn-PCN displayed two weak SOD-like and POD-like activities, they were not switchable. It was presumably because different substrates competed and subsequently interfered at the same Cu/Zn-N_x site in carbon nitride-based dual metal (photo)catalyst. Interestingly, although single higher SOD activity of Cu/GO and light-responsive POD activity of

TiO_2 were observed (**Fig. 3d**), none of them exhibited a similar switch effect as Cu/Zn-C_6N_6 under the light on/off. Then, the above two Cu/GO and TiO_2 catalysts, were mixed into a nanocomposite (Cu/GO-TiO_2). As displayed in **Fig. 3d**, Cu/GO-TiO_2 showed a higher SOD activity under light off and a remarkable light-switchable POD activity; however, the SOD activity always remained when light irradiation. The result demonstrated the Cu/GO-TiO_2 was not applicable for reversible switch between SOD- and POD-like activities because the former was unable to realize the remarkably inhibition under light irradiation. It was supposed that the same active center in Cu/Zn-C_6N_6 realized the inhibition and activation of disparate enzyme activities by alternating light on and off, thus highly switching the SOD and POD reactions, which resembled with the behavior of the inhibition and activation of multienzyme activity through allosteric regulation.

Moreover, the cyclic experiment was conducted to study SOD-/POD like activity recovery of Cu/Zn-C_6N_6. As shown in **Fig. S22**, in the first several cycles of light on and off, SOD-like activity was not only reversibly recovered but also activated to a higher performance, reaching a maximum $O_2^{\cdot-}$ elimination of 78%, which demonstrated that light irradiation can activate more active centers of Cu/Zn-N_x. Similarly, POD-like activity also gradually increased and reached a plateau with several cycle of light on and off (**Fig. S23**). Moreover, the high reversibility of the switch at the optimal activity was demonstrated by measuring the absorbance after repetitive alternating light on and off (**Fig. 3e**). These results indicated that after activation Cu/Zn-C_6N_6 had a stable cycling ability, achieving a highly reversible switch between SOD-/POD-like activities triggered by light.

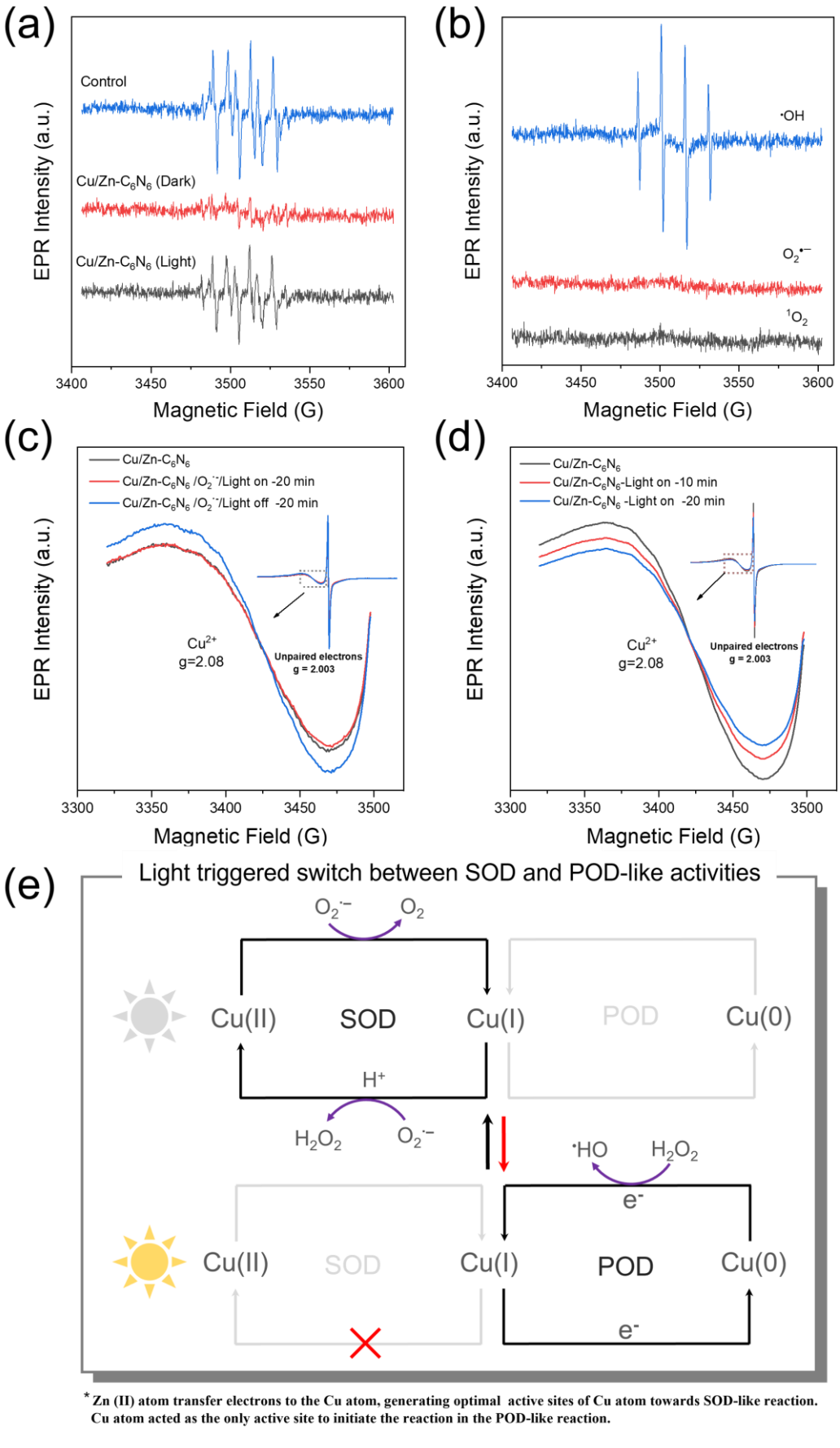

* Zn (II) atom transfer electrons to the Cu atom, generating optimal active sites of Cu atom towards SOD-like reaction. Cu atom acted as the only active site to initiate the reaction in the POD-like reaction.

Fig. 4 Mechanism of reversible transformation between SOD- and POD-like activity by

Cu/Zn-C_6N_6. (a) EPR spectra of the spin adduct of $O_2^{\cdot-}$ generated in xanthine/xanthine oxidase system with/without Cu/Zn-C_6N_6 with light on or off. (b) EPR spectra of the spin adduct of ·OH, $O_2^{\cdot-}$, and $^1O_2$ generated during the activation of H_2O_2 by Cu/Zn-C_6N_6. *In-situ* solid EPR spectra change of Cu^{2+} in Cu/Zn-C_6N_6 under (c) SOD and (d) POD-like reactions: dry powder (black) and loaded on capillary tube recorded by controlling light on or off at given time intervals. (e) Proposed switch mechanism of SOD-like and POD-like activities for Cu/Zn-C_6N_6 mimicking cycles between different metal oxidation states.

Mechanism of reversible transformation between SOD- and POD-like activity by Cu/Zn-C_6N_6

To understand the mechanism for reversible transformation of SOD and POD-like activity by Cu/Zn-C_6N_6, the possible intermediate reactive species were investigated in the first set experiments by electron spin resonance (ESR). As displayed in **Fig. 4a**, the control ESR spectrum showed a typical peak of DMPO- $O_2^{\cdot-}$ spin adduct (blue line), which possessed four spectral lines with a relative intensity of 1:1:1:1 in the xanthine/xanthine oxidase system.[71] When Cu/Zn-C_6N_6 was present, the DMPO-$O_2^{\cdot-}$ adduct decreased sharply (red line), confirming the strong elimination ability of $O_2^{\cdot-}$. In contrast, under the light irradiation, the intensity of DMPO-$O_2^{\cdot-}$ adduct only slightly reduced, indicating that the SOD-like activity of Cu/Zn-C_6N_6 was remarkedly inhibited. Interestingly, under light irradiation, there was a typical characteristic peak of the DMPO-•OH spin adduct with a typical signal intensity of 1:2:2:1 in catalytical oxidation ABTS by Cu/Zn-C_6N_6, a typical fact of decomposition of the H_2O_2 to •OH, indicating the switch to a POD-like activity. Scavenger trapping experiments and other trapping experiments were also studied to confirm the above results (**Fig. S24** and **Fig. S25**). Therefore, two typical $O_2^{\cdot-}$ and •OH intermediates were exclusively observed in SOD-/POD-like reactions by Cu/Zn-C_6N_6 under dark and light on conditions, respectively.

The *in situ* ESR monitoring the valence states of Cu in Cu/Zn-C_6N_6 was further explored during the SOD-like reaction with/without light irradiation (**Fig. 4c**). Given that Cu^{2+} had a much stronger ESR intensity in the air at g = 2.08 (black line),[34] and as the reaction progressed, the Cu^{2+} signal increased gradually when the light was off,

indicating the higher content of Cu^{2+} was formed from Cu^{+} during the SOD-like reaction. Notably, when the SOD-like reaction was under light irradiation, the change of Cu signal became negligible, and even slightly decreased, which demonstrated SOD-like activity of Cu/Zn-C_6N_6 was restrained. In contrast, the valence states of Cu^{2+} in Cu/Zn-C_6N_6 displayed a reverse phenomenon in the POD-like reaction (**Fig. 4d**). Before irradiation, the ESR spectrum of Cu/Zn-C_6N_6 exhibited a strong signal of Cu^{2+}. It decreased with the irradiation time increase (0-30 min), which demonstrated that the photoelectron of Cu^{2+} occurred in the C_6N_6 framework, resulting in the formation of ESR-silent Cu^{+} during light irradiation.[72] Moreover, to further investigate the chemical-bond evolution of Cu/Zn-C_6N_6 in SOD-/POD-like reactions, XPS spectroscopy was performed to clarify the dynamic changes of Cu-N. As shown in **Fig. S26a**, Cu $2p^{3/2}$ initially appeared to be composed of two peaks at around 931.9 (Cu^{+}, 51 %) and 934.8 (Cu^{2+}, 49 %) eV. After SOD-like reaction, the Cu^{+} content decreased from 51 to 38 %, while the percentage of Cu^{2+} increased from 49 to 62%, which was attributed to the partial oxidation of Cu^{+} to Cu^{2+}. Interestingly, after light irradiation, Cu^{2+} reduced from 49 to 39 % and the ratio of Cu^{+} and Cu^{0} increased from 51 to 61% (**Fig. S26b**), further suggesting the acceptance of photoelectrons for Cu atoms in the switch POD reaction. Therefore, the valence state of Cu with cycling between 2+ and 1+ during the SOD-like reaction by Cu/Zn-C_6N_6 under dark, while it switched to cycle between 1+ and 0 for POD-like reaction by Cu/Zn-C_6N_6 under light irradiation.

Taking above all experimental results into consideration, the mechanism for the SOD-like and light-switched POD-like activity of Cu/Zn-C_6N_6 was proposed in **Fig. 4e**. Briefly, in the SOD-like reaction, owing to a Zn-doped synergistic effect, Cu acted as the main catalytic active site. $O_2^{\cdot-}$ was adsorbed on the Cu^{2+}-N_2/Zn^{2+}-N_2 coordination metal site in Cu/Zn-C_6N_6, and bound to form Cu^{2+}-N_2-$O_2^{\cdot-}$/Zn^{2+}-N_2. Subsequently, Cu^{2+}-N_2/Zn^{2+}-N_2 turned into Cu^{+}-N_2/Zn^{2+}-N_2 with slight changes in the valence state while oxidizing $O_2^{\cdot-}$ to oxygen, which dissociated into the system (**Eq. 1**). Next, another molecule $O_2^{\cdot-}$ was further adsorbed to the Cu^{+}-N_2/Zn^{2+}-N_2 site, forming Cu^{+}-N_2-$O_2^{\cdot-}$/Zn^{2+}-N_2, and finally it was reduced to generate H_2O_2 with combined two H atoms,

while Cu^{+}-N_2/Zn^{2+}-N_2 is oxidized to recover the Cu^{2+}-N_2/Zn^{2+}-N_2 (**Eq. 2**). This result indicated Cu valence states alternatively cycled between +2 and +1 in continuous encounters with $O_2^{\cdot-}$ during the SOD-like catalytic reaction, which is similar to the action of natural Cu/Zn-SOD enzymes.[73, 74] In contrast, when the light was on, the photocatalytic processes were activated to switch the other catalytic activity (**Eq. 3**). The single Cu active species acted as acceptance of photogenerated electrons, and these photoelectrons subsequently reduced Cu^{+} to Cu^{0} (**Eq. 4**). Next, the H_2O_2 was in situ decomposed by Cu^{0} to generate $^{\cdot}OH$ via a Fenton-like process. Finally, Cu^{0} was also oxidized by H_2O_2 to facilitate the formation of Cu^{+} species (**Eq. 5**), completing the photocatalytic valence states cycle between +1 and 0.[45, 75] Therefore, for Cu/Zn-C_6N_6, the multiformity of the cycles between different valence state for the same catalytic active center made the reaction activity capable of being highly reversible conversion, which outperformed the multi-enzyme activity of natural enzymes to a certain extent.

Reversible switching sensing of xanthine and glucose in cell mimics

The management of chronic diseases like diabetes and gout remains a significant challenge in healthcare. Both conditions share common pathogenic precursors, namely glucose and xanthine. Growing research interest focuses on sensing these metabolites as a potential early diagnostic biomarker for disease prevention. In recent years, many nanozyme-based biosensing strategies of glucose and xanthine have been reported,[1, 17, 45, 76, 77] due to their simplicity, sensitivity, and high selectivity. Despite significant progress, multiple individual biosensors in response to glucose and xanthine are still needed. The intelligent detection of both glucose and xanthine without crosstalk on a single sensing interface is highly anticipated to boost sensing operation efficiency but remains a grand challenge.

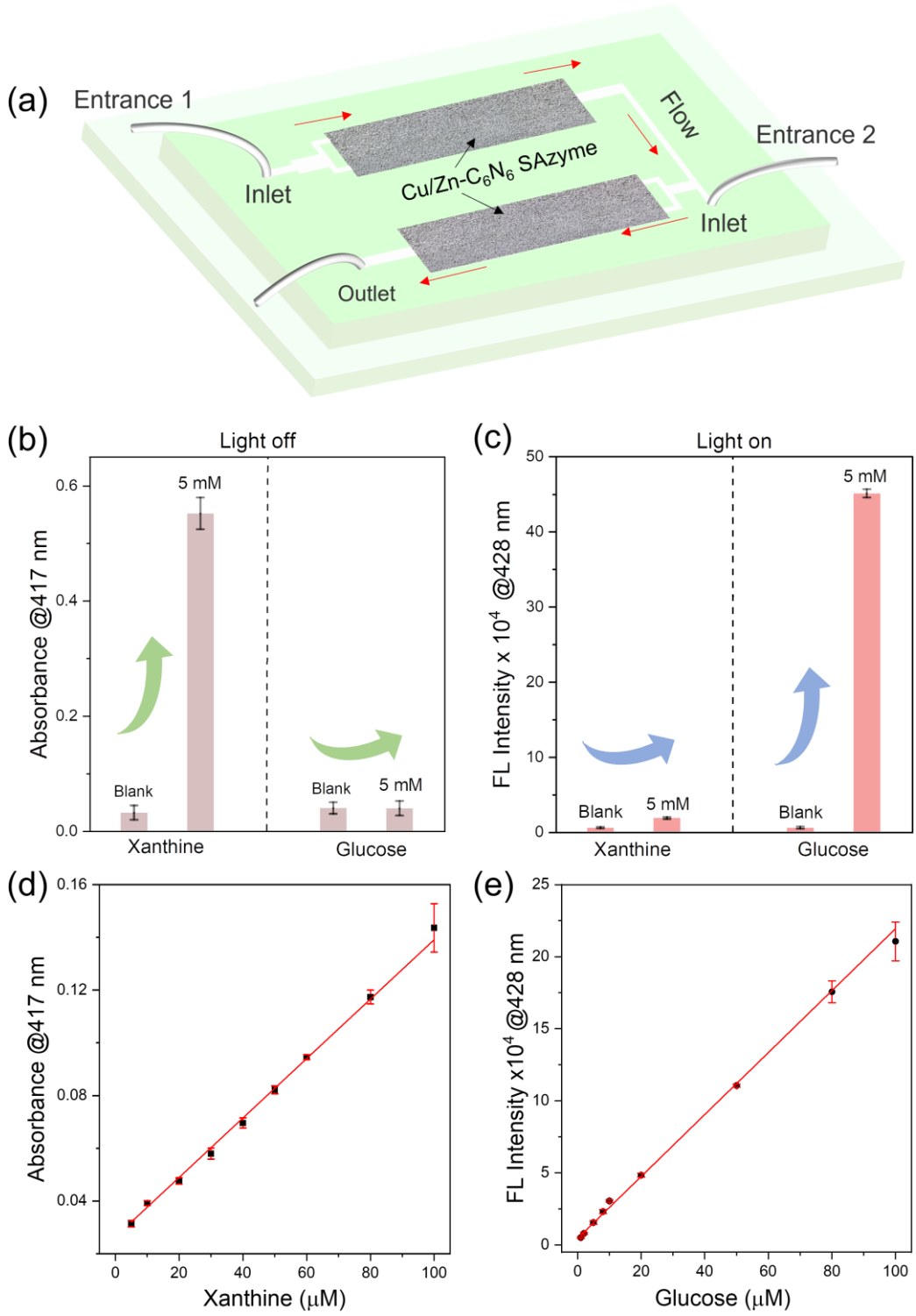

Fig. 6 Adaptable xanthine and glucose biosensor in microfluidics. (a) Schematic configuration of adaptable biosensors in a microfluidic device. (b) Absorbance of the $ABTS_{ox}$ and (c) the FL intensity of •OH-TPA increased with Xanthine and Glucose in the SOD and POD-like reaction. Calibration curves of xanthine in the dark (d) and glucose under light irradiation (e).

As a proof of concept, we proposed an intelligent switch sensor for alternatingly monitoring glucose and xanthine in a continuous flow microfluidic reactor, in which the above SOD-like and POD-like reactions would be promoted with enhanced mass transfer. Moreover, it was able to miniaturize the system, became a portable real-time monitoring platform, and simulate the basic behavior of cells. As shown in **Fig. 6a**, a feasible microfluidic device for xanthine (light off) and glucose (light on) switchable detection was constructed by stacking a PDMS substrate with Cu/Zn-C_6N_6-coated microfluidic channels on a glass slide. When the light was off, different concentrations of xanthine and xanthine oxidase were injected into Entrance 1, subsequently, $O_2^{\cdot-}$ was catalyzed to form H_2O_2 in the Cu/Zn-C_6N_6-coated channel. Next, the horseradish peroxidase (HRP)/ABTS was injected into Entrance 2 to meet the flowing H_2O_2 and finally, the ABTS was oxidized forming $ABTS_{ox}$. The outflow of $ABTS_{ox}$ was measured using an online UV visible spectrometer at 417 nm (**Fig. S27a**). Similarly, under light irradiation, different concentrations of glucose and glucose oxidase/TPA were injected into Entrance 1 and Entrance 2, respectively. When H_2O_2 generated by the glucose/glucose oxidase flowed through the light channel, Cu/Zn-C_6N_6 with activated POD-like activity catalyzed it to generate $^{\cdot}OH$ via a Fenton-like process, which reacted with the TPA to form $^{\cdot}OH$-TPA. The $^{\cdot}OH$-TPA can be subjected to fluorescent monitoring at the emission wavelength of 428 nm (**Fig. S28a**).

Fig. 6b and **c** graphically illustrate the advantage of switchable biosensor for alternatingly monitoring xanthine and glucose. When the light was off, the generation rate of $ABTS_{ox}$ increased with the increase in xanthine concentration (**Fig. S27b**), while the generation of $ABTS_{ox}$ with increased glucose was negligible. In contrast to the inhibition of SOD-like reaction, glucose showed a remarkable enhancement effect on $^{\cdot}OH$-TPA production (**Fig. S28b**), promoting POD-like reaction catalysis under light irradiation. Moreover, the strict nonlinear rate equations (**Fig. S27c and Fig. S28c**) under the modified and original Michaelis-Menten mechanism[78] were used to match the experimental data well in the full-scale analyte concentrations of xanthine and glucose, and the detected linear range of two were 5-100 μM and 1-100 μM with a

detection limit of 1.62 μM and 0.35 μM (**Fig. 6c, d**). Those results showed that Cu/Zn-C_6N_6 -based intelligent sensor successfully realized the switchable response of xanthine (light off) and glucose (light on), enabled by the mimic allosteric regulation of Cu/Zn-C_6N_6 using reversible and efficient conversion of SOD-like and POD-like reactions.

It should be mentioned that although several nanozymes-based biosensors have been reported,[79-81] to our knowledge, the intelligent switch biosensors with mimic allosteric regulation have been rarely reported so far. Unlike most multiple-function systems that have "always on" activities in the off-state, limiting the precise inhibition and recovery of enzyme-like reactions. Cu/Zn-C_6N_6 exhibited alternating SOD-like and POD-like activity, reminiscent of the feature of the inhibition and activation of multienzyme activity through allosteric regulation in the metabolic process. Moreover, space constraints in intelligent artificial devices often limit the number of deployable biosensors. Mechanical switching for different analyses further reduces operational efficiency. Therefore, a single biosensor capable of reversible and efficient conversion of enzyme-like activities triggered by light is highly desirable. It is foreseeable that further considering the intrinsic outstanding temporal and spatial resolution of light irradiation, this intelligent biosensor would supply a prospective candidate for dynamic chemical noses for intelligent artificial devices, such as robots, brain-machine interface, and internet-to-things in a high level of integration.

Conclusion

In summary, we proposed a graphitic C_6N_6-based dual Cu/Zn single-atom catalyst with a synergistic effect to address the mismatch of catalytic center between enzyme and photocatalysis in simulating the allosteric regulation function of natural enzymes through switching the different valence cycling. Cu/Zn-C_6N_6 could not only eliminate superoxide anions ($O_2^{\cdot-}$) through the superoxide dismutase-like (SOD) reaction but also switch oxidation of peroxidase-like (POD) substrates under light irradiation, at the same time, SOD-like activity was inhibited. Furthermore, when the light was stopped, SOD-

like activity was resumed. Notably, the shared same active center (Cu/Zn-N_x) for enzyme-like catalysis and photocatalysis displayed different forms of the cycle between different oxidation states. The former was preferred to follow the on-cycle of Cu(I/II)/Zn(II) owing to the synergistic effect, while the latter activated the Cu(I)/Cu(0) cycle. The multiformity of the cycle between different valence state cycles for the same catalytic active center made the reaction activity capable of reversible and efficient conversion. As a result, an elimination efficiency of $O_2^{\cdot-}$ about 78% and a 30-fold increase in POD-like activity under light irradiation were obtained. The light-switched efficiency can reach more than 90%. As a proof-of-concept application, Cu/Zn-C_6N_6 was successfully applied to a single intelligent switch biosensor for alternatingly monitoring glucose and xanthine in a continuous flow microfluidic reactor, simply by turning the light on. It is highly anticipated that graphitic C_6N_6-based dual Cu/Zn single-atom nanozyme, along with the further intrinsic temporal and spatial resolution of light, would supply a prospective candidate for adaptable chemical noses for artificial devices, such as robots, brain-machine interface, and internet to things, in a higher level of integration.

Acknowledgements

This work was supported by the National Natural Science Foundation of China (22174014, 22074015), and the Fundamental Research Funds for the Central Universities.

Conflict of interest

The authors declare no conflict of interest.

References

1. Zhu, C.; Zhou, Z.; Gao, X. J.; Tao, Y.; Cao, X.; Xu, Y.; Shen, Y.; Liu, S.; Zhang, Y., Cascade nanozymatic network mimicking cells with selective and linear perception of H_2O_2. *Chem. Sci.* **2023,** *14*, 6780-6791.

2. Cheng, W.; Wang, X.; Xiong, Z.; Liu, J.; Liu, Z.; Jin, Y.; Yao, H.; Wong, T.-S.; Ho, J. S.; Tee, B. C. K., Frictionless multiphasic interface for near-ideal aero-elastic pressure sensing. *Nat. Mater.* **2023,** *22*, 1352-1360.

3. Xu, H.; Wu, S.; Liu, Y.; Wang, X.; Efremov, A. K.; Wang, L.; McCaskill, J. S.; Medina-Sánchez, M.; Schmidt, O. G., 3D nanofabricated soft microrobots with super-compliant picoforce springs as onboard sensors and actuators. *Nat. Nanotech.* **2024**, https://doi.org/10.1038/s41565-023-01567-0.

4. Kim, T. Y.; Hong, S. H.; Jeong, S. H.; Bae, H.; Cheong, S.; Choi, H.; Hahn, S. K., Multifunctional Intelligent Wearable Devices Using Logical Circuits of Monolithic Gold Nanowires. *Adv. Mater.* **2023,** *35*, 2303401.

5. Khan, S.; Monteiro, J. K.; Prasad, A.; Filipe, C. D. M.; Li, Y.; Didar, T. F., Material Breakthroughs in Smart Food Monitoring: Intelligent Packaging and On-Site Testing Technologies for Spoilage and Contamination Detection. *Adv. Mater.* **2023,** *36*, 2300875.

6. Gao, L.; Zhuang, J.; Nie, L.; Zhang, J.; Zhang, Y.; Gu, N.; Wang, T.; Feng, J.; Yang, D.; Perrett, S.; Yan, X., Intrinsic peroxidase-like activity of ferromagnetic nanoparticles. *Nat. Nanotech.* **2007,** *2*, 577-583.

7. Chen, Y.; Ji, S.; Chen, C.; Peng, Q.; Wang, D.; Li, Y., Single-Atom Catalysts: Synthetic Strategies and Electrochemical Applications. *Joule* **2018,** *2*, 1242-1264.

8. Jiao, L.; Yan, H.; Wu, Y.; Gu, W.; Zhu, C.; Du, D.; Lin, Y., When Nanozymes Meet Single-Atom Catalysis. *Angew. Chem. Int. Ed.* **2019,** *59*, 2565-2576.

9. Wu, J.; Wang, X.; Wang, Q.; Lou, Z.; Li, S.; Zhu, Y.; Qin, L.; Wei, H., Nanomaterials with enzyme-like characteristics (nanozymes): next-generation artificial enzymes (II). *Chem. Soc. Rev.* **2019,** *48*, 1004-1076.

10. Huang, Y.; Ren, J.; Qu, X., Nanozymes: Classification, Catalytic Mechanisms, Activity Regulation, and Applications. *Chem. Rev.* **2019,** *119*, 4357-4412.

11. Qiao, B.; Wang, A.; Yang, X.; Allard, L. F.; Jiang, Z.; Cui, Y.; Liu, J.; Li, J.; Zhang, T., Single-atom catalysis of CO oxidation using Pt_1/FeO_x. *Nat. Chem.* **2011,** *3*, 634-641.

12. Wu, W.; Huang, L.; Wang, E.; Dong, S., Atomic engineering of single-atom nanozymes for enzyme-like catalysis. *Chem. Sci.* **2020,** *11*, 9741-9756.

13. Peng, C.; Pang, R.; Li, J.; Wang, E., Current Advances on the Single-Atom Nanozyme and Its Bioapplications. *Adv. Mater.* **2023**, 2211724.

14. Ji, S.; Jiang, B.; Hao, H.; Chen, Y.; Dong, J.; Mao, Y.; Zhang, Z.; Gao, R.; Chen, W.; Zhang, R.; Liang, Q.; Li, H.; Liu, S.; Wang, Y.; Zhang, Q.; Gu, L.; Duan, D.; Liang, M.; Wang, D.; Yan, X.; Li, Y., Matching the kinetics of natural enzymes with a single-atom iron nanozyme. *Nat. Catal.* **2021,** *4*, 407-417.

15. Chen, Z.; Mitchell, S.; Vorobyeva, E.; Leary, R. K.; Hauert, R.; Furnival, T.; Ramasse, Q. M.; Thomas, J. M.; Midgley, P. A.; Dontsova, D.; Antonietti, M.; Pogodin, S.; López, N.; Pérez-Ramírez, J., Stabilization of Single Metal Atoms on Graphitic Carbon Nitride. *Adv. Funct. Mater.* **2017,** *27*, 1605785.

16. Wang, Y.; Mao, J.; Meng, X.; Yu, L.; Deng, D.; Bao, X., Catalysis with Two-Dimensional Materials Confining Single Atoms: Concept, Design, and Applications. *Chem. Rev.* **2018,** *119*, 1806-1854.

17. Zhang, P.; Sun, D.; Cho, A.; Weon, S.; Lee, S.; Lee, J.; Han, J. W.; Kim, D.-P.; Choi, W., Modified carbon nitride nanozyme as bifunctional glucose oxidase-peroxidase for metal-free bioinspired cascade photocatalysis. *Nat. Commun.* **2019,** *10*, 940.

18. Vázquez-González, M.; Liao, W.-C.; Cazelles, R.; Wang, S.; Yu, X.; Gutkin, V.; Willner, I., Mimicking Horseradish Peroxidase Functions Using Cu^{2+}-Modified Carbon Nitride Nanoparticles or Cu^{2+}-Modified Carbon Dots as Heterogeneous Catalysts. *ACS Nano* **2017,** *11*, 3247-3253.

19. Jiao, L.; Xu, W.; Yan, H.; Wu, Y.; Liu, C.; Du, D.; Lin, Y.; Zhu, C., Fe–N–C Single-Atom Nanozymes for the Intracellular Hydrogen Peroxide Detection. *Anal. Chem.* **2019,** *91*, 11994-11999.

20. Xu, Y.; Xue, J.; Zhou, Q.; Zheng, Y.; Chen, X.; Liu, S.; Shen, Y.; Zhang, Y., The Fe-N-C Nanozyme with Both Accelerated and Inhibited Biocatalytic Activities Capable of Accessing Drug–Drug Interactions. *Angew. Chem. Int. Ed.* **2020,** *59*, 14498-14503.

21. Ju, E.; Dong, K.; Chen, Z.; Liu, Z.; Liu, C.; Huang, Y.; Wang, Z.; Pu, F.; Ren, J.; Qu, X., Copper(II)-Graphitic Carbon Nitride Triggered Synergy: Improved ROS Generation and Reduced Glutathione Levels for Enhanced Photodynamic Therapy. *Angew. Chem. Int. Ed.* **2016,** *55*, 11467-11471.

22. Wang, Y.; Jia, G.; Cui, X.; Zhao, X.; Zhang, Q.; Gu, L.; Zheng, L.; Li, L. H.; Wu, Q.; Singh, D. J.; Matsumura, D.; Tsuji, T.; Cui, Y.-T.; Zhao, J.; Zheng, W., Coordination Number Regulation of Molybdenum Single-Atom Nanozyme Peroxidase-like Specificity. *Chem* **2021,** *7*, 436-449.

23. Wang, D.; Wu, H.; Phua, S. Z. F.; Yang, G.; Qi Lim, W.; Gu, L.; Qian, C.; Wang, H.; Guo, Z.; Chen, H.; Zhao, Y., Self-assembled single-atom nanozyme for enhanced photodynamic therapy treatment of tumor. *Nat. Commun.* **2020,** *11*, 357.

24. Zhang, X.; Lin, S.; Huang, R.; Gupta, A.; Fedeli, S.; Cao-Milán, R.; Luther, D. C.; Liu, Y.; Jiang, M.; Li, G.; Rondon, B.; Wei, H.; Rotello, V. M., Degradable ZnS-Supported Bioorthogonal Nanozymes with Enhanced Catalytic Activity for Intracellular Activation of Therapeutics. *J. Am. Chem. Soc.* **2022,** *144*, 12893-12900.

25. Zhang, S.; Li, Y.; Sun, S.; Liu, L.; Mu, X.; Liu, S.; Jiao, M.; Chen, X.; Chen, K.; Ma, H.; Li, T.; Liu, X.; Wang, H.; Zhang, J.; Yang, J.; Zhang, X.-D., Single-atom nanozymes catalytically surpassing naturally occurring enzymes as sustained stitching for brain trauma. *Nat. Commun.* **2022,** *13*, 4744.

26. Wang, D.; Zhao, Y., Single-atom engineering of metal-organic frameworks toward healthcare. *Chem* **2021,** *7*, 2635-2671.

27. Xiang, H.; Feng, W.; Chen, Y., Single-Atom Catalysts in Catalytic Biomedicine. *Adv. Mater.* **2020,** *32*, 1905994.

28. Zhang, R.; Xue, B.; Tao, Y.; Zhao, H.; Zhang, Z.; Wang, X.; Zhou, X.; Jiang, B.; Yang, Z.; Yan, X.; Fan, K., Edge-Site Engineering of Defective Fe–N_4 Nanozymes with Boosted Catalase-Like Performance for Retinal Vasculopathies. *Adv. Mater.* **2022,** *34*, 2205324.

29. Yang, J.; Zhang, R.; Zhao, H.; Qi, H.; Li, J.; Li, J. F.; Zhou, X.; Wang, A.; Fan, K.; Yan, X.; Zhang, T., Bioinspired copper single-atom nanozyme as a superoxide dismutase-like antioxidant for sepsis treatment. *Exploration* **2022,** *2*, 210267.

30. Xu, W.; Zhong, H.; Wu, Y.; Qin, Y.; Jiao, L.; Sha, M.; Su, R.; Tang, Y.; Zheng, L.; Hu, L.; Zhang, S.; Beckman, S. P.; Gu, W.; Yang, Y.; Guo, S.; Zhu, C., Photoexcited Ru single-atomic sites for efficient biomimetic redox catalysis. *P. Acad. Nat. Sci.* **2023,** *120*, 20315120.

31. Ma, C. B.; Xu, Y.; Wu, L.; Wang, Q.; Zheng, J. J.; Ren, G.; Wang, X.; Gao, X.; Zhou, M.; Wang, M.; Wei, H., Guided Synthesis of a Mo/Zn Dual Single-Atom Nanozyme with Synergistic Effect and Peroxidase-like Activity. *Angew. Chem. Int. Ed.* **2022,** *61*, 2116170.

32. Gao, W.; He, J.; Chen, L.; Meng, X.; Ma, Y.; Cheng, L.; Tu, K.; Gao, X.; Liu, C.; Zhang, M.; Fan, K.; Pang, D.-W.; Yan, X., Deciphering the catalytic mechanism of superoxide dismutase activity of carbon dot nanozyme. *Nat. Commun.* **2023,** *14*, 160.

33. Xu, Y.; Zhou, Z.; Deng, N.; Fu, K.; Zhu, C.; Hong, Q.; Shen, Y.; Liu, S.; Zhang, Y., Molecular insights of nanozymes from design to catalytic mechanism. *Sci. Chi. Chem.* **2023,** *66*, 1318-1335.

34. Hai, X.; Zheng, Y.; Yu, Q.; Guo, N.; Xi, S.; Zhao, X.; Mitchell, S.; Luo, X.; Tulus, V.; Wang, M.; Sheng, X.; Ren, L.; Long, X.; Li, J.; He, P.; Lin, H.; Cui, Y.; Peng, X.; Shi, J.; Wu, J.; Zhang, C.; Zou, R.; Guillén-Gosálbez, G.; Pérez-Ramírez, J.; Koh, M. J.; Zhu, Y.; Li, J.; Lu, J., Geminal-atom catalysis for cross-coupling. *Nature* **2023,** *622* (7984), 754-760.

35. Wang, F.; Zhang, Y.; Du, Z.; Ren, J.; Qu, X., Designed heterogeneous palladium catalysts for reversible light-controlled bioorthogonal catalysis in living cells. *Nat. Commun.* **2018,** *9*, 1209.

36. Sahoo, J.; Sahoo, S.; Subramaniam, Y.; Bhatt, P.; Rana, S.; De, M., Photo-Controlled Gating of Selective Bacterial Membrane Interaction and Enhanced Antibacterial Activity for Wound Healing. *Angew. Chem. Int. Ed.* **2023,** *63*, 2314804.

37. Neri, S.; Garcia Martin, S.; Pezzato, C.; Prins, L. J., Photoswitchable Catalysis by a Nanozyme Mediated by a Light-Sensitive Cofactor. *J. Am. Chem. Soc.* **2017,** *139*, 1794-1797.

38. Dong, H.; Du, W.; Dong, J.; Che, R.; Kong, F.; Cheng, W.; Ma, M.; Gu, N.; Zhang, Y., Depletable peroxidase-like activity of Fe_3O_4 nanozymes accompanied with separate migration of electrons and iron ions. *Nat. Commun.* **2022,** *13*, 5365.

39. Xu, J.; Zhang, Q.; Gao, X.; Wang, P.; Che, H.; Tang, C.; Ao, Y., Highly Efficient FeIII-initiated Self-cycled Fenton System in Piezo-catalytic Process for Organic Pollutants Degradation. *Angew. Chem. Int. Ed.* **2023,** *62*, 2307018.

40. Wan, K.; Jiang, B.; Tan, T.; Wang, H.; Liang, M., Surface-Mediated Production of Complexed •OH Radicals and Fe=O Species as a Mechanism for Iron Oxide Peroxidase-Like Nanozymes. *Small* **2022,** *18*, 2204372.

41. Chen, X.; Zhao, L.; Wu, K.; Yang, H.; Zhou, Q.; Xu, Y.; Zheng, Y.; Shen, Y.; Liu, S.; Zhang, Y., Bound oxygen-atom transfer endows peroxidase-mimic M–N–C with high substrate selectivity. *Chem. Sci.* **2021,** *12*, 8865-8871.

42. Herget, K.; Hubach, P.; Pusch, S.; Deglmann, P.; Götz, H.; Gorelik, T. E.; Gural'skiy, I. y. A.; Pfitzner, F.; Link, T.; Schenk, S.; Panthöfer, M.; Ksenofontov, V.; Kolb, U.; Opatz, T.; André, R.; Tremel, W., Haloperoxidase Mimicry by CeO_{2-x} Nanorods Combats Biofouling. *Adv. Mater.* **2017,** *29*, 1603823.

43. Ragg, R.; Natalio, F.; Tahir, M. N.; Janssen, H.; Kashyap, A.; Strand, D.; Strand, S.; Tremel, W., Molybdenum Trioxide Nanoparticles with Intrinsic Sulfite Oxidase Activity. *ACS Nano* **2014,** *8*, 5182-5189.

44. Zhang, W.; Hu, S.; Yin, J.-J.; He, W.; Lu, W.; Ma, M.; Gu, N.; Zhang, Y., Prussian Blue Nanoparticles as Multienzyme Mimetics and Reactive Oxygen Species Scavengers. *J. Am. Chem. Soc.* **2016,** *138*, 5860-5865.

45. Hong, Q.; Yang, H.; Fang, Y.; Li, W.; Zhu, C.; Wang, Z.; Liang, S.; Cao, X.; Zhou, Z.; Shen, Y.; Liu, S.; Zhang, Y., Adaptable graphitic C_6N_6-based copper single-atom catalyst for intelligent biosensing. *Nat. Commun.* **2023,** *14*, 2780.

46. Celardo, I.; Pedersen, J. Z.; Traversa, E.; Ghibelli, L., Pharmacological potential of cerium oxide nanoparticles. *Nanoscale* **2011,** *3*, 1411-1420.

47. Huang, G.-Z.; Xia, Y.-S.; Yang, F.; Long, W.-J.; Liu, J.-J.; Liao, J.-P.; Zhang, M.; Liu, J.; Lan, Y.-Q., On–Off Switching of a Photocatalytic Overall Reaction through Dynamic Spin-State Transition in a Hofmann Clathrate System. *J. Am. Chem. Soc.* **2023,** *145*, 26863-26870.

48. Wu, S.-G.; Wang, L.-F.; Ruan, Z.-Y.; Du, S.-N.; Gómez-Coca, S.; Ni, Z.-P.; Ruiz, E.; Chen, X.-M.; Tong, M.-L., Redox-Programmable Spin-Crossover Behaviors in a Cationic Framework. *J. Am. Chem. Soc.* **2022,** *144*, 14888-14896.

49. Gong, Y.-N.; Zhong, W.; Li, Y.; Qiu, Y.; Zheng, L.; Jiang, J.; Jiang, H.-L., Regulating Photocatalysis by Spin-State Manipulation of Cobalt in Covalent Organic

Frameworks. *J. Am. Chem. Soc.* **2020,** *142*, 16723-16731.

50. Du, Z.; Meng, Z.; Gong, X.; Hao, Z.; Li, X.; Sun, H.; Hu, X.; Yu, S.; Tian, H., Rapid Surface Reconstruction of Pentlandite by High-Spin State Iron for Efficient Oxygen Evolution Reaction. *Angew. Chem. Int. Ed.* **2024**, e202317022.

51. Gao, Y.; Wang, J.; Yang, Y.; Wang, J.; Zhang, C.; Wang, X.; Yao, J., Engineering Spin States of Isolated Copper Species in a Metal–Organic Framework Improves Urea Electrosynthesis. *Nano-Micro Lett.* **2023,** *15*, 158.

52. Day, C. S.; Rentería-Gómez, Á.; Ton, S. J.; Gogoi, A. R.; Gutierrez, O.; Martin, R., Elucidating electron-transfer events in polypyridine nickel complexes for reductive coupling reactions. *Nat. Catal.* **2023,** *6*, 244-253.

53. Huang, C.; Wen, Y.; Ma, J.; Dong, D.; Shen, Y.; Liu, S.; Ma, H.; Zhang, Y., Unraveling fundamental active units in carbon nitride for photocatalytic oxidation reactions. *Nat. Commun.* **2021,** *12*, 320.

54. Wang, J.; Chen, Y.; Shen, Y.; Liu, S.; Zhang, Y., Coupling polymorphic nanostructured carbon nitrides into an isotype heterojunction with boosted photocatalytic H_2 evolution. *Chem. Commun.* **2017,** *53*, 2978-2981.

55. Wang, H.; Jiang, D.; Huang, D.; Zeng, G.; Xu, P.; Lai, C.; Chen, M.; Cheng, M.; Zhang, C.; Wang, Z., Covalent triazine frameworks for carbon dioxide capture. *J. Mater. Chem. A* **2019,** *7*, 22848-22870.

56. Xie, J.; Shevlin, S. A.; Ruan, Q.; Moniz, S. J. A.; Liu, Y.; Liu, X.; Li, Y.; Lau, C. C.; Guo, Z. X.; Tang, J., Efficient visible light-driven water oxidation and proton reduction by an ordered covalent triazine-based framework. *Environ. Eng. Sci.* **2018,** *11*, 1617-1624.

57. Devautour-Vinot, S.; Maurin, G.; Serre, C.; Horcajada, P.; Paula da Cunha, D.; Guillerm, V.; de Souza Costa, E.; Taulelle, F.; Martineau, C., Structure and Dynamics of the Functionalized MOF Type UiO-66(Zr): NMR and Dielectric Relaxation Spectroscopies Coupled with DFT Calculations. *Chem. Mater.* **2012,** *24*, 2168-2177.

58. Zhu, X.; Tian, C.; Mahurin, S. M.; Chai, S.-H.; Wang, C.; Brown, S.; Veith, G. M.; Luo, H.; Liu, H.; Dai, S., A Superacid-Catalyzed Synthesis of Porous Membranes Based on Triazine Frameworks for CO_2 Separation. *J. Am. Chem. Soc.* **2012,** *134*, 10478-

10484.

59. Zhao, T.; Zhou, Q.; Lv, Y.; Han, D.; Wu, K.; Zhao, L.; Shen, Y.; Liu, S.; Zhang, Y., Ultrafast Condensation of Carbon Nitride on Electrodes with Exceptional Boosted Photocurrent and Electrochemiluminescence. *Angew. Chem. Int. Ed.* **2019,** *59*, 1139-1143.

60. Yang, J.; Liu, W.; Xu, M.; Liu, X.; Qi, H.; Zhang, L.; Yang, X.; Niu, S.; Zhou, D.; Liu, Y.; Su, Y.; Li, J.-F.; Tian, Z.-Q.; Zhou, W.; Wang, A.; Zhang, T., Dynamic Behavior of Single-Atom Catalysts in Electrocatalysis: Identification of Cu-N_3 as an Active Site for the Oxygen Reduction Reaction. *J. Am. Chem. Soc.* **2021,** *143*, 14530-14539.

61. Sun, T.; Li, Y.; Cui, T.; Xu, L.; Wang, Y.-G.; Chen, W.; Zhang, P.; Zheng, T.; Fu, X.; Zhang, S.; Zhang, Z.; Wang, D.; Li, Y., Engineering of Coordination Environment and Multiscale Structure in Single-Site Copper Catalyst for Superior Electrocatalytic Oxygen Reduction. *Nano Lett.* **2020,** *20*, 6206-6214.

62. Tong, M.; Sun, F.; Xie, Y.; Wang, Y.; Yang, Y.; Tian, C.; Wang, L.; Fu, H., Operando Cooperated Catalytic Mechanism of Atomically Dispersed Cu−N_4 and Zn−N_4 for Promoting Oxygen Reduction Reaction. *Angew. Chem. Int. Ed.* **2021,** *60*, 14005-14012.

63. Xu, F.; Meng, K.; Cheng, B.; Wang, S.; Xu, J.; Yu, J., Unique S-scheme heterojunctions in self-assembled TiO_2/$CsPbBr_3$ hybrids for CO_2 photoreduction. *Nat. Commun.* **2020,** *11*, 4613.

64. Zhang, L.; Li, T.; Dai, X.; Zhao, J.; Liu, C.; He, D.; Zhao, K.; Zhao, P.; Cui, X., Water Activation Triggered by Cu−Co Double-Atom Catalyst for Silane Oxidation. *Angew. Chem. Int. Ed.* **2023,** *62*, 2313343.

65. Zhang, T.; Zhang, D.; Han, X.; Dong, T.; Guo, X.; Song, C.; Si, R.; Liu, W.; Liu, Y.; Zhao, Z., Preassembly Strategy To Fabricate Porous Hollow Carbonitride Spheres Inlaid with Single Cu–N_3 Sites for Selective Oxidation of Benzene to Phenol. *J. Am. Chem. Soc.* **2018,** *140*, 16936-16940.

66. Liu, H.; Li, X.; Ma, Z.; Sun, M.; Li, M.; Zhang, Z.; Zhang, L.; Tang, Z.; Yao, Y.; Huang, B.; Guo, S., Atomically Dispersed Cu Catalyst for Efficient Chemoselective Hydrogenation Reaction. *Nano Lett.* **2021,** *21*, 10284-10291.

67. Li, J.; Chen, S.; Yang, N.; Deng, M.; Ibraheem, S.; Deng, J.; Li, J.; Li, L.; Wei, Z.,

Ultrahigh-Loading Zinc Single-Atom Catalyst for Highly Efficient Oxygen Reduction in Both Acidic and Alkaline Media. *Angew. Chem. Int. Ed.* **2019,** *58*, 7035-7039.

68. Xu, B.; Wang, H.; Wang, W.; Gao, L.; Li, S.; Pan, X.; Wang, H.; Yang, H.; Meng, X.; Wu, Q.; Zheng, L.; Chen, S.; Shi, X.; Fan, K.; Yan, X.; Liu, H., A Single-Atom Nanozyme for Wound Disinfection Applications. *Angew. Chem. Int. Ed.* **2019,** *58*, 4911-4916.

69. Rahim, M. A.; Tang, J.; Christofferson, A. J.; Kumar, P. V.; Meftahi, N.; Centurion, F.; Cao, Z.; Tang, J.; Baharfar, M.; Mayyas, M.; Allioux, F.-M.; Koshy, P.; Daeneke, T.; McConville, C. F.; Kaner, R. B.; Russo, S. P.; Kalantar-Zadeh, K., Low-temperature liquid platinum catalyst. *Nat. Chem.* **2022,** *14*, 935-941.

70. Xi, J.; Zhang, R.; Wang, L.; Xu, W.; Liang, Q.; Li, J.; Jiang, J.; Yang, Y.; Yan, X.; Fan, K.; Gao, L., A Nanozyme-Based Artificial Peroxisome Ameliorates Hyperuricemia and Ischemic Stroke. *Adv. Funct. Mater.* **2020,** *31*, 2007130.

71. Lu, M.; Wang, J.; Ren, G.; Qin, F.; Zhao, Z.; Li, K.; Chen, W.; Lin, Y., Superoxide-like Cu/GO single-atom catalysts nanozyme with high specificity and activity for removing superoxide free radicals. *Nano Res.* **2022,** *15*, 8804-8809.

72. Luo, L.; Han, X.; Wang, K.; Xu, Y.; Xiong, L.; Ma, J.; Guo, Z.; Tang, J., Nearly 100% selective and visible-light-driven methane conversion to formaldehyde via. single-atom Cu and $W^{\delta+}$. *Nat. Commun.* **2023,** *14*, 2690.

73. Sheng, Y.; Abreu, I. A.; Cabelli, D. E.; Maroney, M. J.; Miller, A.-F.; Teixeira, M.; Valentine, J. S., Superoxide Dismutases and Superoxide Reductases. *Chem. Rev.* **2014,** *114*, 3854-3918.

74. Zhao, H.; Zhang, R.; Yan, X.; Fan, K., Superoxide dismutase nanozymes: an emerging star for anti-oxidation. *J. Mater. Chem. B* **2021,** *9*, 6939-6957.

75. Zhou, Y.; Zhang, L.; Wang, W., Direct functionalization of methane into ethanol over copper modified polymeric carbon nitride via photocatalysis. *Nat. Commun.* **2019,** *10*, 506.

76. Wei, H.; Wang, E., Fe_3O_4 Magnetic Nanoparticles as Peroxidase Mimetics and Their Applications in H_2O_2 and Glucose Detection. *Anal. Chem.* **2008,** *80*, 2250-2254.

77. Wang, Q.; Zhang, X.; Huang, L.; Zhang, Z.; Dong, S., GOx@ZIF-8(NiPd)

Nanoflower: An Artificial Enzyme System for Tandem Catalysis. *Angew. Chem. Int. Ed.* **2017,** *56*, 16082-16085.

78. Hong, Q.; Shen, Y.; Liu, S.; Zhang, Y., Re-Examination of Plotting Analytical Response against Different Forms of Concentration. *Anal. Chem.* **2021,** *93*, 11910-11914.

79. Cao, X.; Zhu, C.; Hong, Q.; Chen, X.; Wang, K.; Shen, Y.; Liu, S.; Zhang, Y., Insight into Iron Leaching from an Ascorbate-Oxidase-like Fe−N−C Nanozyme and Oxygen Reduction Selectivity. *Angew. Chem. Int. Ed.* **2023,** *62*, 2302463.

80. Li, W.; Zhang, M.; Han, D.; Yang, H.; Hong, Q.; Fang, Y.; Zhou, Z.; Shen, Y.; Liu, S.; Huang, C.; Zhu, H.; Zhang, Y., Carbon Nitride-Based Heterojunction Photoelectrodes with Modulable Charge-Transfer Pathways toward Selective Biosensing. *Anal. Chem.* **2023,** *95*, 13716-13724.

81. Zhu, C.; Yang, H.; Cao, X.; Hong, Q.; Xu, Y.; Wang, K.; Shen, Y.; Liu, S.; Zhang, Y., Decoupling of the Confused Complex in Oxidation of 3,3′,5,5′-Tetramethylbenzidine for the Reliable Chromogenic Bioassay. *Anal. Chem.* **2023,** *95*, 16407-16417.